Journal of Materials Chemistry A

Accepted Manuscript

ROYAL SOCIETY OF CHEMISTRY

www.rsc.org/materialsA

Beaded Manganese Oxide (Mn_2O_3) Nanofibers: Preparation and Application for Capacitive Energy Storage

Muhamed Shareef Kolathodi[1,3*], Samerender Nagam Hanumantha Rao[1,2], Tirupattur Srinivasan Natarajan[1], Gurpreet Singh[3]

[1]*Conducting Polymer Lab, Department of Physics, Indian Institute of Technology Madras, Chennai - 600036, India Fax: +91- 44 22574852; Tel: +91- 4422574860;*

[*]*Email: muhamed@ksu.edu*

[2]*Department of Biomedical Engineering, Michigan Technological University, Houghton, MI 49931, USA*

[3]*Department of Mechanical and Nuclear Engineering, Kansas State University, Manhattan, Kansas 66506, United States Tel.: +1-785-532-7085; Fax: +1-785-532-7057.*

Keywords: Energy storage; Supercapacitor; Electrochemical properties; Electrospinning; Nanofiber; Mn_2O_3

Abstract: Here we report a surfactant-free electrospinning based method for the synthesis of beaded manganese oxide (Mn_2O_3) nanofibers and application as supercapacitor electrode. Beaded morphology of the fibers was confirmed through electron microscopic analysis. High crystalline nature and lattice strain of the fibers were verified by X-ray diffraction analysis while chemical composition of the fibers was studied by use of X-ray photoelectron and Raman Spectroscopy. Electrochemical properties of Mn_2O_3 nanofiber electrode were investigated using cyclic voltammetry, galvanostatic charge/discharge, and electrochemical impedance

spectroscopy in a 0.5 M Na_2SO_4 aqueous electrolyte. The specific capacitance of the Mn_2O_3 beaded nanofibers was found to be 358 Fg^{-1} at a current density of 0.5 Ag^{-1}. Lattice strain-induced ionic and electronic defects enhanced the surface properties of the Mn_2O_3 nanofibers, thereby improving the electrochemical properties.

1. Introduction

The growing energy crisis and increasing environmental pollution necessitate research on eco-friendly energy conversion and efficient storage devices. Compared to batteries and fuel cells, supercapacitors (SCs) are suitable alternative energy storage devices due to their high-power density, long cycle life, fast charge/discharge rate, cost effectiveness, and eco-friendly nature.[1-3] Recent progress has emphasized increasing the power density and capacitance of SCs.[4] However, development of electrode materials with high surface areas are crucial in order for SCs to achieve high energy and power densities with excellent rate capability and prolonged lifespan.[5,6] Electrode materials for SCs are currently comprised of transition metal oxides (TMOs),[7,8] metal sulfides,[9,10] carbon-based materials,[11,12] conducting polymers,[13] and combinations of metal-carbon-based material.[14-16] TMOs such as RuO_2, Fe_3O_4, CoO_x, NiO, TiO_2 and MnO_x have been proposed as suitable electrode materials due to their high theoretical capacitance and good cycling stability compared to those based on carbon and conducting polymers.[17-21] Among TMOs, manganese oxides (MnO_x) have several benefits, such as high theoretical specific capacitance (~1370 Fg^{-1} at 1 V), multiple oxidation states, environmentally friendly nature, natural abundance, and inexpensive.[22-24]

Although MnO_x has many advantages over other TMOs, its decreased electrical conductivity and stability make bulk MnO_x inadequate for use as electrodes in SCs. However, this inadequacy can be overcome by stepping into nanoscale dimension of the active materials

and creating hybrids with carbonaceous materials such as activated carbon, carbon nanotubes, or graphene.[25] In addition to the double layer capacitance of hybrids, high surface-to-volume ratio of nanostructures increases the available area of electrolyte for charge storage by intercalating ions and redox reactions. These synergic effects eventually increase the observed capacitance. As a result, previous works on MnO_x nanostructure electrodes have shown improved capacitive rate-retention.[26-28] It is well known that the method of synthesis influences the surface area, density of states, surface-to-volume ratio, and crystalline phases of the nanostructure. Synthesis methods currently in use include top-down and bottom-up approaches such as lithographic patterning techniques, sol-gel processing, solvothermal synthesis, chemical vapor deposition, electrospinning etc.[29] Among these techniques, electrospinning is arguably the simplest and most cost-effective procedure for preparation of a wide range of nanofibers (NFs). Sol-gel preparation before electrospinning is most advantageous because homogeneous mixing of reactants at the molecular level enables control over the shape, size, and morphology.[30, 31]

Various morphologies of Mn_2O_3 and its hybrids have been reported as high performance electrode for SC applications. For example, hybrid manganese oxide films (Mn_2O_3 and Mn_3O_4) synthesized by Lin et al. delivered a specific capacitance of 340.3 Fg^{-1} with a reduced retention (82.5%) after 100 cycles.[32] Electrospun MnO_x NFs and its hybrids, such as MnO_x/CNT and MnO_x/SnO, delivered a specific capacitance of 166 Fg^{-1}, 182 Fg^{-1}, and 472 Fg^{-1}, respectively, however the retention and energy density were very low.[33] Wei et al. reported synthesis of confined manganese oxides within carbon nanotubes (CNTs) for SC applications with a specific capacitance of 225 Fg^{-1}.[34] Similarly, electrospun MnO_x NFs synthesized by Eunhee et al. exhibited a specific capacitance of 360.7 Fg^{-1}.[35] Li et al. synthesized a unique morphology of porous Mn_2O_3 nanocubics that exhibited a specific capacitance of 191.1 Fg^{-1} with a rate

capability of 58.6%.[36] More recently, graphene-Mn_2O_3 nanocomposite have been shown to deliver a maximum specific capacitance of 300 Fg^{-1}.[37] Although Ding et al. have reported preparation of Mn_2O_3 nanofibers using polyvinylpyrrolidone and manganese chloride ($MnCl_2$) by electrospinning for hydrazine detection application, the procedure was complicated due to hygroscopic nature of $MnCl_2$, and there was no report of bead formation, strain induced effects, and capacitive energy storage.[38] In the present work we report a cost-effective, surfactant-free method for fabrication of mesoporous, beaded Mn_2O_3 NFs with high crystalline nature using a two-step facile process: electrospinning followed by calcination in air. Electrochemical properties of the beaded NFs for SC applications were studied in aqueous Na_2SO_4 electrolyte. Capacitance and stability were investigated and recorded. To our knowledge, this is the first report of fabrication of Mn_2O_3 beaded NFs for application as electrodes in SCs.

2. Experimental Section

2.1 Preparation of Mn_2O_3 Nanofibers

Manganese acetate (MnAc) and poly (vinylalcohol) (PVA, molecular weight 125,000) were procured from Merck (India) Ltd. and Central Drug House (P) Ltd., India, respectively. Acetylene black (99% purity), poly(vinylidene fluoride) (PVDF) and N-methylpyrrolidinone (NMP) were purchased from Sigma-Aldrich. All chemicals were used as received without further purification. MnAc (0.26 g) was initially dissolved in deionized water (4 mL) in the weight ratio (6.1%). The polymer (PVA) of weight 0.5 g was homogenously dispersed in as-prepared MnAc solution by stirring for 5 h. Electrospun fibers were prepared with the ESPIN - NANO designed and developed in our lab indigenously and manufactured by Physics Equipment Co. Chennai, India. The sol-gel was used for electrospinning under the following conditions: tip-

to-collector distance of 15 cm, electric potential of 15 kV, and flow rate of 0.5 mL h^{-1}. As-spun composite fibers were subjected to calcination in air at 700 °C for 1 h with a heating rate of 2 °C min^{-1}.

2.2 Characterization of Electrospun Structures

Physicochemical characterizations were performed using X-ray diffraction (XRD), thermogravimetric analysis (TGA), differential scanning calorimetry (DSC), Raman spectroscopy, nitrogen adsorption isotherms, X-ray photoelectron spectroscopy (XPS), and microscopic techniques. XRD patterns were collected in the range 15°–70° using PANalytical X′PERT Pro X-ray diffractometer equipped with nickel-filtered Cu K_α radiation (λ = 1.542 Å). The oxidation state and elemental composition were investigated using an XPS system (Omicron NanoTechnology, Germany) with a monochromatic Al K_α X-ray source (1486.7 eV). Surface morphology of the NFs was revealed via field emission scanning electron microscopy (FESEM) (FEI Quanta FEG 400 at 15 kV) and transmission electron microscope (TEM, Philips CM 20 TEM at 120 kV). Horiba Jobin Yvon HR 800 (total magnification of 1000 and resolution of 2 cm^{-1}) was used to record the Raman spectrum using a He-Ne laser of wavelength 632.8 nm. A Micromeritics ASAP 2020 Porosimeter was used to obtain nitrogen adsorption isotherms of NFs measured at -195.66 °C.

2.3 Electrochemical Measurements

Initially, Mn_2O_3 NFs (electrode material), acetylene black (conducting agent), and PVDF (binder) were dispersed in NMP with a weight ratio of 80:15:5, respectively, in order to make slurry. The slurry was brush-coated on a stainless steel plate in order to obtain electrochemical characterizations of the electrode material in 0.5 M Na_2SO_4 electrolyte using a three-electrode

setup. For symmetric cell design, the working electrodes were prepared by coating the slurry (1 mg) on Toray carbon paper over an area of 1 cm^2. A Whatman filter paper pretreated in the electrolyte was sandwiched between two such electrodes. Electrochemical properties were investigated using Ivium CompactStat (Ivium Technologies, Netherland) at room temperature. Cyclic voltammetry (CV) and galvanostatic charge-discharge (GCD) were performed in the potential range of 0–1V. Electrochemical Impedance Spectrum (EIS) of the device was carried out with an alternating signal of amplitude 5 mV in the frequency range of 1 MHz to 10 mHz at an open circuit potential (OCP).

3. Results and Discussion

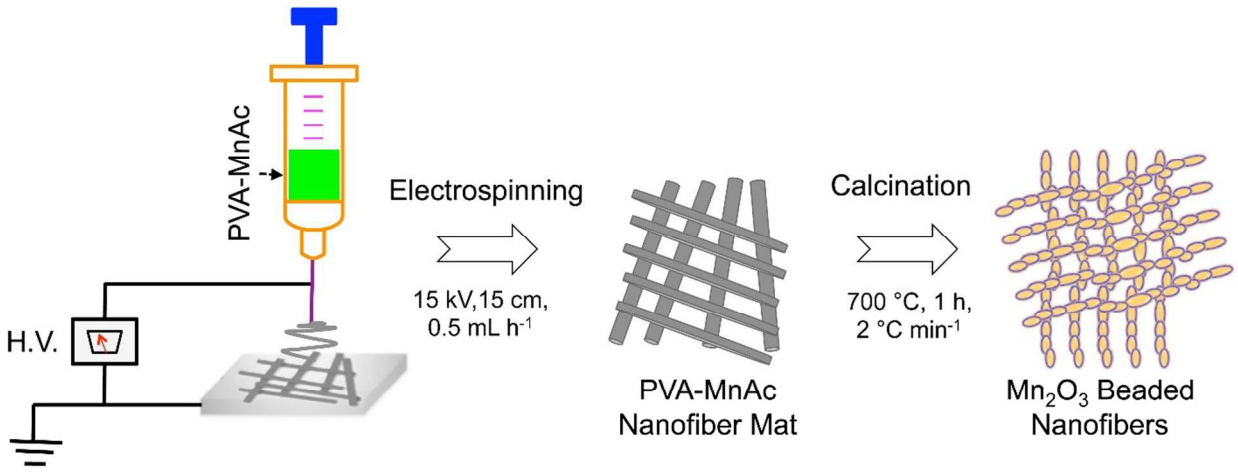

Fig. 1. Schematic of preparation of Mn_2O_3 beaded nanofibers

A schematic of Mn_2O_3 NF preparation is shown in Fig. 1. Figs. 2(a)(i) and 2(a)(ii) show TGA and DSC plots (SDT Q600 TA), respectively, of the as-spun manganese acetate-polyvinyl alcohol (MnAc-PVA) composite fibers taken within a temperature range of 30–700 °C at a heating rate of 20 °C min^{-1}. As a control experiment, the TGA and DSC of pure PVA fibers were carried out in air, as shown in Fig. S1 of the Supporting information (SI). The decomposition of

MnAc and PVA proceeded in three steps. In the first step, dehydration of MnAc occurred in the temperature range 100–190 °C, and weight loss at 190 °C was found to be 74%. In the second step, decomposition of PVA and MnAc started after 230 °C and the process of decomposition continued up to 480 °C. The complete decomposition of PVA and MnAc occurred below 500 °C, and weight loss was found to be ~29%, which correlates with the literature data.[39] This 29 % weight corresponds to both Mn_2O_3 and amorphous carbon, where carbon content was 4% as revealed in the TGA of pure PVA fibers (Fig. S1 of SI). Therefore, a higher calcination temperature (700 °C) was chosen to ensure that all volatile (H_2O, CO_x, etc.) and organic constituents due to PVA and the acetate group was evaporated. The annealing temperature below 500 °C leads to amorphous oxides as well.[40] The DSC plot in Fig. 2(a)(ii) shows three endothermic peaks below ~364 ºC due to loss of absorbed H_2O, decomposition of MnAc, and pyrolysis of PVA due to dehydration of polymer side chains.[41] Below 500 °C, the peak corresponded to the decomposition of the main chain of PVA, in agreement with data obtained from TGA. The crystallinity and composition were corroborated by XRD measurements.

Fig. 2(b) shows the XRD pattern of Mn_2O_3 NFs. All reflections in this pattern could be readily indexed to the cubic phase of Mn_2O_3 with estimated lattice constant a = 0.9417 nm, which are in good agreement with standard reports (JCPDS No.41-1442). This pattern shows that the product was highly crystalline in nature without any other oxides of manganese. Major reflection peaks can be readily indexed to crystal planes of (2 1 1), (2 2 2), (4 0 0), (3 3 2), (4 3 1), (4 4 0), (6 1 1), (5 4 1), (6 2 2), and (6 3 1) of Mn_2O_3. The annealing temperature and environment (air) is one of the reasons for the formation of Mn_2O_3 and not Mn_3O_4 or MnO_2. However, trace quantities of these oxides exist but the dominant oxidation state is Mn(III). The calcination temperature plays a role for the increase in intensity of the peaks of Mn_2O_3 in

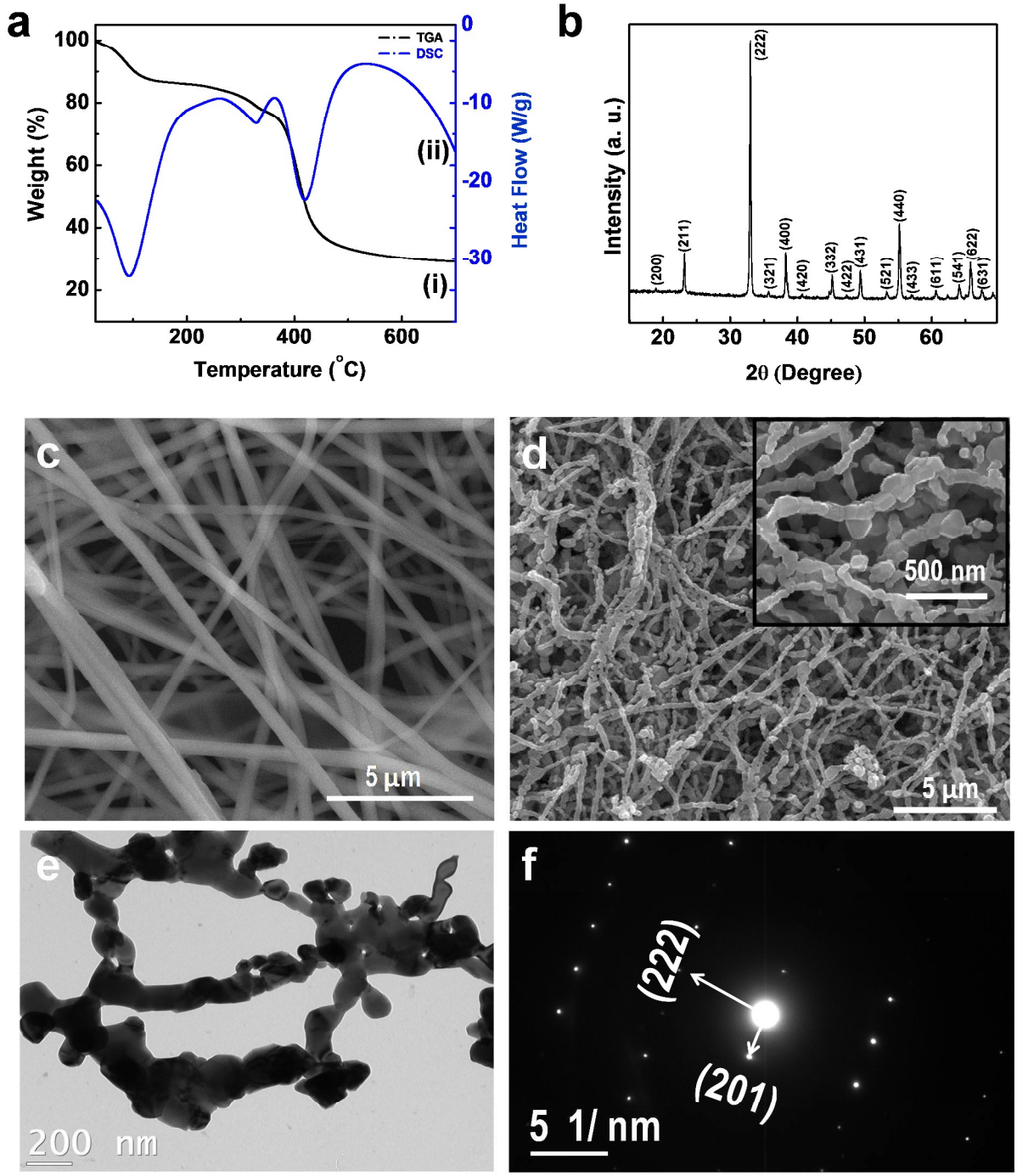

Fig. 2 (a) TGA and DSC plots of as-spun MnAc-PVA nanofibers; (**b)** XRD pattern of Mn_2O_3 nanofibers calcined at 700 °C (JCPDS No.41-1442); **(c)** FESEM images of as-spun MnAc-PVA fibers and **(d)** Mn_2O_3 nanofibers; **(e)** TEM image and**(f)** SAED pattern of Mn_2O_3 nanofibers.

comparison to other oxides of manganese as evident from the existing literature. Annealing in inert atmospheres generally leaves the metallic salt into pure metal and in the particular case

here, the product will be pure manganese fibers.[42-44] Using the Scherrer formula and Williamson Hall plot, the crystallite size and lattice strain were calculated as 45 nm and 0.0031, respectively.[45-48] Peak intensities relatively decreased due to amorphous carbon in the NFs after calcination. Because lattice strain causes atomic vacancies, as reported by Li et al,[49] the sample demonstrated some ionic and electronic defects that enhanced the surface properties of the Mn_2O_3 NFs.[50] Atomic defects also caused a change in the bulk modulus or strain in the atomic bonds.[51] The XRD analysis of the as-spun PVA fibers was carried out for comparison and shown in Fig. S2 of SI. The pattern presents no observable peaks, thereby confirming the amorphous nature of the as-spun fibers.

Morphological analysis of as-spun and heat-treated fibers was characterized by FESEM and TEM analyses. As-spun MnAc-PVA fibers, shown Fig. 2(c), were smooth and thick with an average diameter of 470 nm. Figs. 2(d) and 2(e) show FESEM and TEM images of calcined Mn_2O_3 NFs. As shown in the figures, diameters of calcined fibers decreased and were distributed in the range 40–200 nm. Compared to as-spun fibers, calcined fibers are rough and thin due to the decomposition of polymer template and other organic components during calcination. These NFs were formed from beads of Mn_2O_3 that were obtained in uneven sizes (average bead size ~150 nm, inset of Fig. 2(d)). The bead-like structures helped increase the surface area of the NFs. TEM images and a selected area electron diffraction (SAED) pattern (Figs. 2(e) and 2(f), respectively) were utilized to further study the morphology and crystallinity of the fibers. Average diameters of the beads calculated from TEM analysis were ~200 nm, demonstrating good agreement with SEM observation. Sharp diffraction spots in the SAED pattern indicated the crystalline nature of Mn_2O_3 nanobeads, and the dominant lattice planes were indexed as (2 2 2) and (2 0 1), which further supported the XRD analysis.Strasser et al. demonstrated that lattice

strain can be used to control electrochemical properties of a catalyst in fuel cells.[52] Therefore, the hypothesis was made that lattice strain that develops during bead formation helps to enhance the electrochemical properties of Mn_2O_3 nanobeads.

Multipoint Brunauer-Emmett-Teller (BET) and Barrett-Joyner-Halenda (BJH) analyses were used to determine the specific surface area and pore size distributions of the Mn_2O_3 nanobeads, as shown in Fig. 3(a). The estimated surface area was 26 m^2g^{-1}, with average pore size of 11.9 nm and average pore volume of 0.015037 cm^3g^{-1}. A strong hysteresis loop was evident, as is characteristic of porous materials.[53] The decreased porosity was due to the irregular size and distribution of beads that arose during slow calcination. Raman spectra of the Mn_2O_3 nanobeads were collected and shown in Fig. 3(b). Bands detected at 176 and 270, 486 to 586, and 632 to 657 cm^{-1} can be attributed to the out-of-plane bending modes, asymmetric stretching of oxygen species (Mn-O-Mn) and symmetric stretching modes of Mn_2O_3, respectively.[54-57] The crystal size obtained using the Scherrer formula can be correlated with the change in vibrational modes, and bands located at 176 and 270 cm^{-1} corresponded to the bigger beads[56]. The intense peak at 657 cm^{-1} suggests that the nanobeads possess characteristics of the **Ia3** space group structure.[58] Shifting and broadening in the Raman peaks can also be attributed to Ruetschi defects, oxygen in pockets, or lattice strain caused due to faults in stacking etc. The increase in lattice strain caused by atomic vacancies is seen by peak broadening as seen from XRD.[23]

Further confirmation about the oxidation states of elements present in the Mn_2O_3 NFs was determined by XPS analysis. Fig. 3(c) shows the survey spectrum in which the elements C, O, and Mn are in their respective oxidation states (Mn 3s, Mn 3p, C 1s, O 1s, and Mn 2p). The

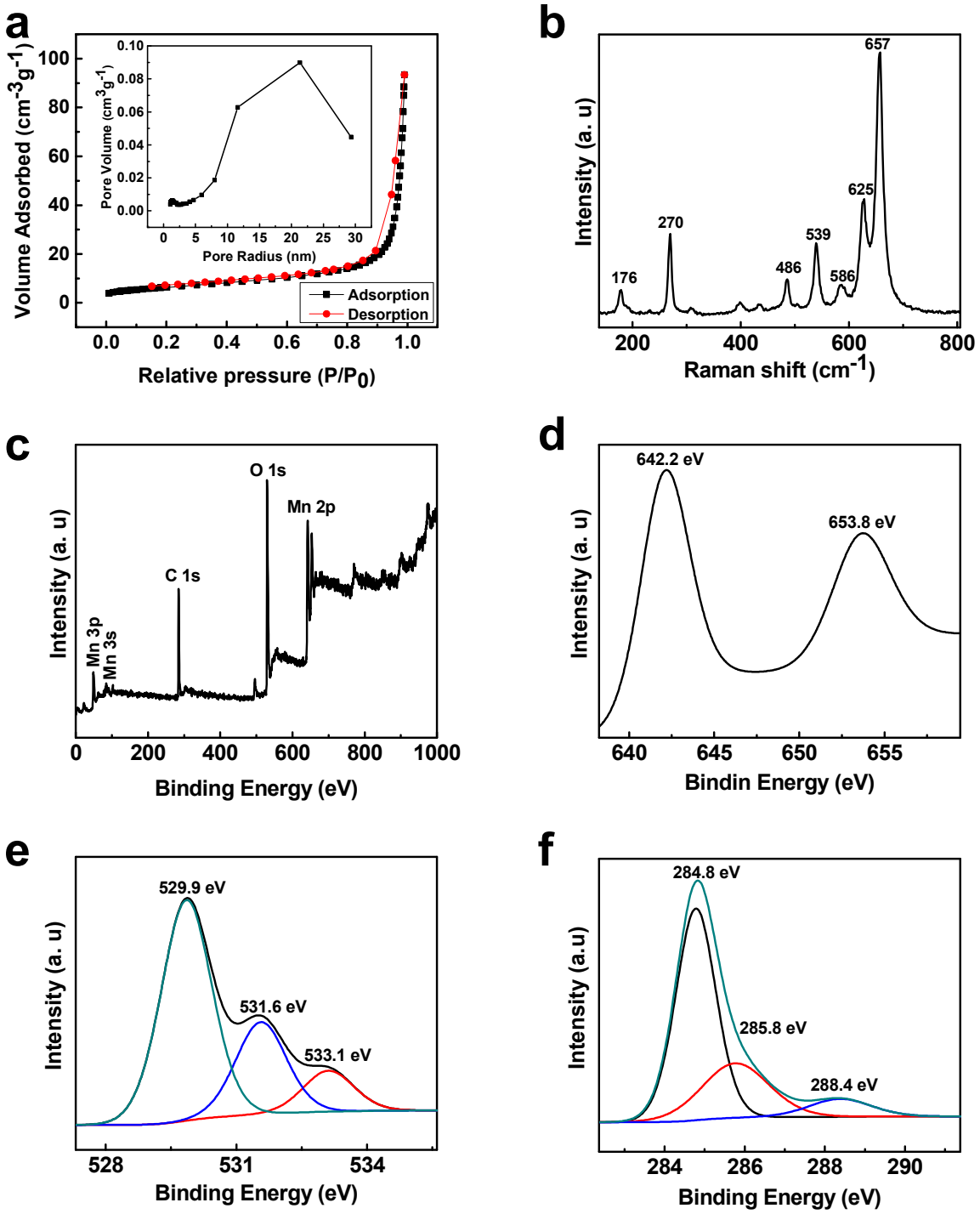

Fig. 3 (a) BET nitrogen adsorption and desorption isotherms of Mn_2O_3 nanofibers with pore size distribution based on BJH method (inset); **(b)** Raman spectrum of Mn_2O_3 NFs excited using a He-Ne laser of wavelength 632.8 nm; **(c–f)** XPS spectrum of Mn_2O_3 nanofibers**: (c)** Survey spectrum; **(d)** Manganese peaks Mn $2p_{3/2}$ (~642.2 eV) and Mn $2p_{1/2}$ (~ 653.8 eV); **(e)** Oxygen (O 1s) assigned to Mn-O-Mn (~529.9 eV), Mn-O-H (~ 531.6 eV), and O-H-O and (~ 533.1 eV); **(f)** Carbon (C 1s) corresponds to C-C (~284.8 eV), C-O-C (~285.8 eV), and O-C=O (~288.4 eV).

peak C 1s could be attributed to the substrate and residual carbon obtained due to the elimination of the polymer matrix. In Fig. 3(d), manganese peaks Mn $2p_{3/2}$ and Mn $2p_{1/2}$ correspond to the energies 642.2 eV and 653.8 eV, respectively, due to spin-orbit splitting. The observed value was ~11.6 eV, which was nearly identical to the band gap energy of Mn^{3+}. Peaks at 284.8 eV, 285.8 eV, and 288.4 eV in Fig. 3(e) could be ascribed to C 1s corresponding to binding energies of C-C, C-O-C, and O-C=O, respectively. Peaks appearing at binding energies of 529.9 eV, 531.6 eV, and 533.1 eV could be assigned to O 1s (Fig. 3(f)), corresponding to Mn-O-Mn, Mn-O-H, and O-H-O, respectively. These observations were in agreement with the literature, and the peaks were curve-fitted.[59,60] XPS and XRD observations confirmed that the NFs were Mn_2O_3. The presence of carbon can be correlated with the decreased intensity of the XRD plots, as shown in Fig. 3(e), which was most likely due to calcination in air rather than calcination in an inert atmosphere.[61] The annealing temperature and the atmosphere provide an essential environment for the formation of nanobeads along with lower loading of MnAc (0.26 g) for 0.5 g of PVA. The limited amount of MnAc acts as a regulatory factor for the formation of beaded structures with mesopores, by stabilizing them at high temperatures. As a control experiment, the loading of MnAc has been varied (0.26, 0.5, 1, and 2 g) and the annealed products (at 700 °C) were Mn_2O_3 in different morphologies (nanobead fiber, nanorods, nano to meso particles, and doughnut shaped particles etc.). The PVA acts as a substrate for the controlled formation of mesopores by stabilizing them at high temperatures.[38,62]

As a promising electrode for SCs, electrochemical properties of the Mn_2O_3 NFs were studied in neutral electrolyte, 0.5 M Na_2SO_4 electrolyte using a three-electrode setup, Ag/AgCl reference electrode and platinum wire counter electrodes. As a control experiment, electrochemical properties of the Mn_2O_3 NFs were studied in alkaline (6M KOH), and acidic

(0.1M H_2SO_4) electrolytes as well. The cyclic voltammograms were recorded at a scan rate of 10 mVs^{-1}, and shown in Fig. S3 of SI. It can be seen from the CV plots that Mn_2O_3 NFs outperforms in 0.5 M Na_2SO_4, compared to acidic and alkaline electrolytes, in terms of both potential window and specific capacitance. The potential windows were 1, 0.8, and 0.5 V in Na_2SO_4, H_2SO_4, and KOH electrolytes, with estimated specific capacitances of 329 Fg^{-1}, 266 Fg^{-1}, and 196 Fg^{-1},

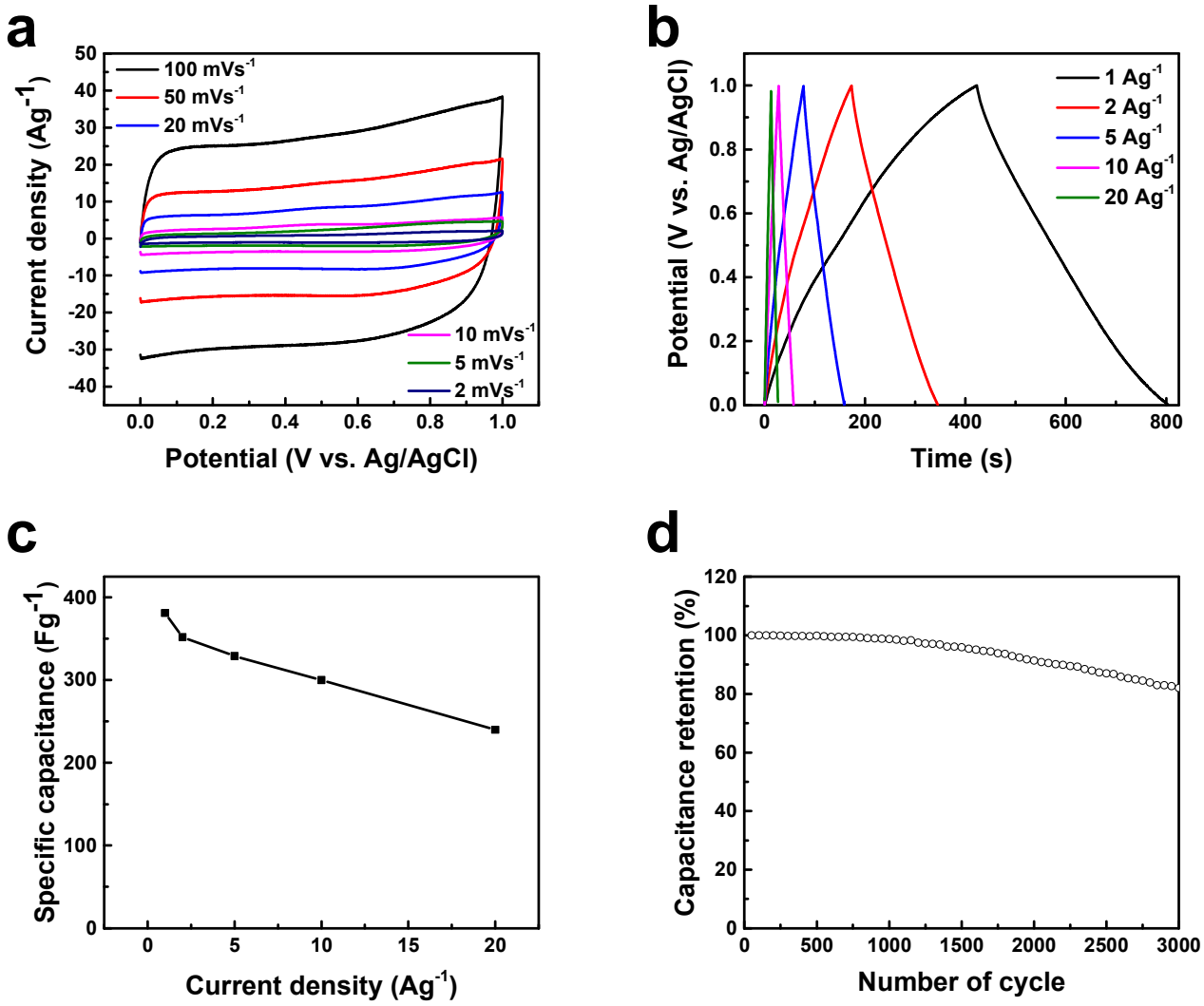

Fig. 4. Electrochemical characterizations of Mn_2O_3 NFs using a three-electrode setup against Ag/AgCl electrode in 0.5 M Na_2SO_4 electrolyte. **(a)** CVs collected at various scan rates; **(b)** GCD plots recorded at various current densities; **(c)** Specific capacitance versus current density; **(d)** Cyclic stability test conducted for 3000 continuous GCD cycles carried out at a current density of 10 Ag^{-1}.

respectively. Therefore, 0.5M Na_2SO_4 electrolyte has been chosen as suitable electrolyte for studying electrochemical properties of the as-prepared Mn_2O_3 NFs for SC application. Fig. 4(a) shows CVs plotted at scan rates of 5–100 mVs^{-1}, and Fig. 4(b) shows GCD plots collected at current densities of 1–20 Ag^{-1}. The rectangular and proportioned CV curves, and symmetrical GCD plots indicate appreciable SC performance and quick charge-discharge process of the beaded NFs. Specific capacitances (C_s) of the electrodes were estimated (in Fg^{-1}) using Equation (1), and plotted in Fig. 4(c).

$$C_s = \frac{I\Delta t}{\Delta V} \qquad (1)$$

where I, Δt, and ΔV represent current density (Ag^{-1}), discharge time (s), and potential window (V), respectively. A maximum specific capacitance of 379 Fg^{-1} was observed at a current density of 1 Ag^{-1}. The electrode material was subjected to a cyclic stability test for 3000 GCD cycles at a current density of 10 Ag^{-1}. The electrode was capable of maintaining 82.6% of its maximum capacitance after 3000 cycles (Fig. 4(d)).

In order to perform practical applications, a symmetric cell was configured with the electrode material and characterized using a two-electrode setup.[63] Fig. 5(a) shows CV plots of the Mn_2O_3 nanofibrous electrode recorded at scan rates of 2, 5, 10, 20, 50, 100, and 200 mVs^{-1} in the voltage window 0–1 V. Corresponding GCD curves were plotted at various current densities of 0.5, 0.75, 1, 2, and 5 Ag^{-1} (Fig. 5(b)). At slow scan rates/current densities, diffusion of ions from the Na_2SO_4 electrolyte could be adsorbed to large areas of the electrodes, leading to complete transfer of ions,[64,65] thereby enhancing redox reactions and specific capacitance of the capacitor.[36] However, the effective electrode-electrolyte interaction decreased significantly at high scan rates/current densities, resulting in reduced specific capacitance, as observed in the rate

capability plot (Fig. 5(c)). The shape of CV curve remained unchanged, indicating excellent SC behavior and fast charging-discharging process that could be attributed to the increased interaction of electrolyte ions on beaded NFs of Mn_2O_3.

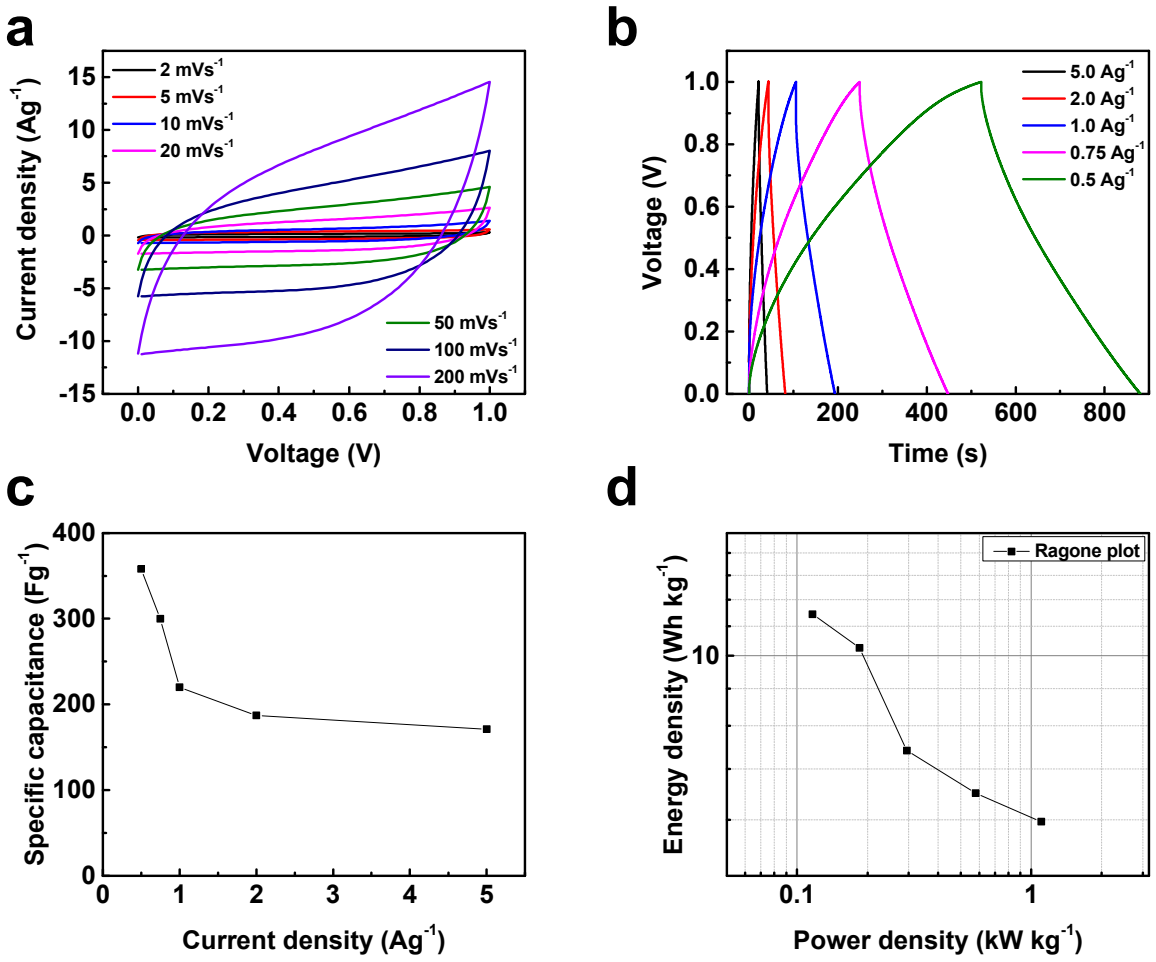

Fig. 5. Electrochemical characterizations of the symmetrical cell designed from Mn_2O_3-based electrodes. **(a)** CV curves collected at various scan rates for a voltage window of 1 V; **(b)** GCD plots recorded at various current densities with a voltage window of 1 V; **(c)** Variation of specific capacitance estimated from GCD plots at various current densities; **(d)** Ragone plot of the symmetric cell.

Thermal treatment-induced lattice strain also enhanced the capacitance by creating lattice defects. The specific capacitance (C_s in Fg^{-1}), energy density (E_s in Wh kg^{-1}), and power density (P_s in kW kg^{-1}) of the electrode material was obtained from the following equations:

$$C_s = 4\frac{C_{cell}}{m} = 4\frac{I\Delta t}{\Delta V} \quad (2)$$

$$E_s = \frac{C_s \Delta V^2}{7.2} \quad (3)$$

$$P_s = \frac{3.6E_s}{t} \quad (4)$$

where C_{cell} is cell capacitance, I is current density (Ag^{-1}), Δt is the time of discharge (s), ΔV is the voltage window after iR drop (V), and m is the total mass of electrode materials in both electrodes (1 mg in each electrode). Highest specific capacitance of 358 Fg^{-1} was observed at a current density 0.5 Ag^{-1}. Fig. 5(d) shows a Ragone plot for the SC; the maximum energy and power densities were 46.39 Wh kg^{-1} and 4.42 kW kg^{-1}, respectively. The highly interconnected, electrospun Mn_2O_3 beaded fibers with high crystallinity and calcination-induced lattice strain significantly enhanced the capacitance and energy density of the SC. In addition, mesopores of the Mn_2O_3 beads introduced an ion buffering effect that improved the electrochemical performance due to increased alignment for insertion and extraction of ions.[66] The entangled nature of the nanobeaded fibers implied increased packing efficiency and subsequently increased electroactive sites for cationic intercalation/de-intercalation with double-layer support.[67,68] Bead-porosity imposed structural stability during charge-discharge cycling, and the presence of carbon, confirmed using XPS analysis, helped in increasing the electrochemical properties of the Mn_2O_3 beaded fibers.

The Nyquist plot can be fitted into a circuit (using ZView 3.0), as shown in Fig. 6(a), with series resistance R_s = 0.4 Ω and charger transfer resistance R_{ct} = 19.4 Ω. The slope of Nyquist plot at a low frequency is increased and tended to become purely capacitive due to the

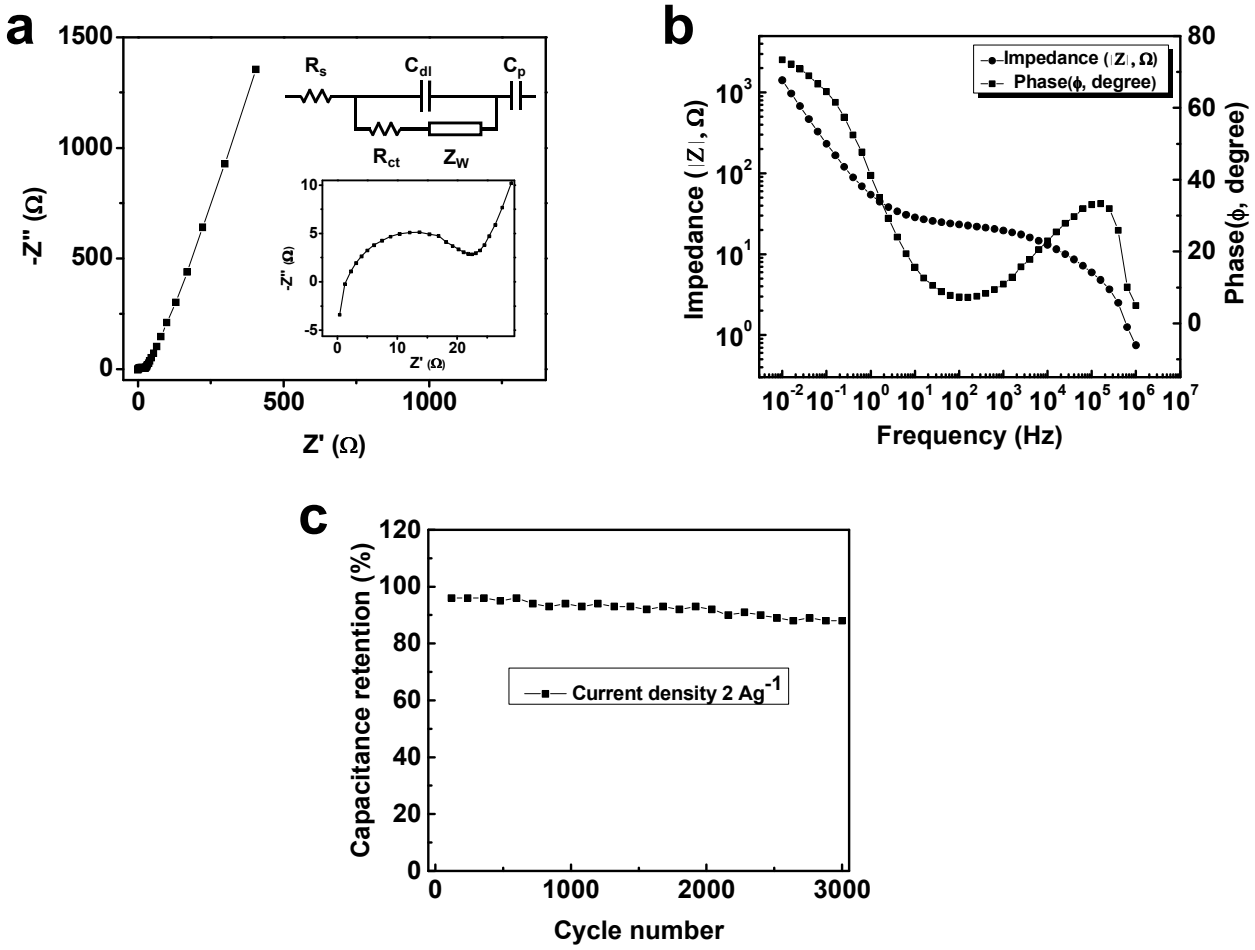

Fig. 6. Electrochemical impedance studies of the Mn_2O_3-based SC carried out in the frequency range 1 MHz to 10 mHz at a signal amplitude of 5 mV under open circuit potential. **(a)** Nyquist plot with equivalent circuit and magnified high frequency region; **(b)** Bode plots of phase angle and impedance versus frequency; **(c)** Cyclic stability test of the symmetric cell carried out at a current density of 2 Ag^{-1} for 3000 GCD cycles.

Warburg impedance, which arose from the frequency dependence of ion diffusion and transport in Na_2SO_4. The large Warburg region indicated a variation in ion diffusion path lengths and increased obstruction of ion movement. From the Bode plot (impedance versus frequency) shown in Fig. 6(b), knee frequency of the SC was estimated to be 0.5 Hz with a relaxation time constant of 2 s. The small time constant corresponded to fast discharging of the total stored energy of the SC. Fig. 6(c) shows SC stability over 3000 charge-discharge cycles carried out at a

current density of 2 Ag^{-1}. It maintained 87.8% of its initial capacitance, thereby demonstrating the high SC cyclic stability. This was the highest capacitance reported with such high stability for the Mn_2O_3-based SCs. The most probable reasons for the increased specific capacitance and power densities are based on the experimental data.

The pseudocapacitive mechanism is dependent on the underpotential deposition, redox, and intercalation pseudocapacitance. The redox and intercalation pseudocapacitance play a major role in the specific capacitance of the nanobeaded electrode material that was directly influenced by the interconnected beaded structure.[69] Nanobeads of crystalline Mn_2O_3 with a thin layer of amorphous carbon provides better pseudocapacitance due to increased utilization of the material and subsequently increased intercalation of ions.[70,71] Percolation is typically higher in beaded architecture than nano arrays and aligned nanofibers; therefore, nanobeads allow increased ion interaction at the active sites.[72] As shown in the CV plots in Fig. 4(a) and Fig. 5(a), less change in the current density occurred at slow scan rates, particularly at 2 mVs^{-1}, due to the available carbon in the electrodes that can adsorb any hydrogen released during reaction.[73] Moreover, porous morphology of the electrode aids reversible oxidization, thereby increasing the anodic current.[74,75] At higher scan rates, ion movements are limited only to active surfaces of the electrode material, consequently suppressing the cathodic and anodic currents and the capacitance. Nature of the electrolyte also plays a role in increasing specific capacitance. The aqueous Na_2SO_4 electrolyte has higher intercalation rate, and therefore greater percolation occurs inside electrode pores, signifying a decrease in delay and offering considerable supporting for charge storage.[76,77] Table S1 in the supporting information compares the performances of various MnO_x that have been fabricated for use as electrodes in SCs. The prepared electrode material can also be used as an anode in rechargeable lithium ion batteries.[78]

4. Conclusion

Electrospinning and post calcination of manganese acetate-PVA composite fibers were employed for the fabrication of bead-shaped, highly crystalline mesoporous nanofibers of Mn_2O_3 with crystallite sizes of approximately 45 nm. As a favorable candidate for SC electrodes, the electrochemical properties were studied in 0.5 M Na_2SO_4 electrolyte over a voltage window of 0–1 V using both the three-electrode and two-electrode setups. Maximum specific capacitance was estimated to be 358 Fg^{-1} at a current density of 0.5 Ag^{-1}. The SC showed significant reversibility as well as high energy and power densities of 46.39 Wh kg^{-1} and 4.42 kW kg^{-1}, respectively. The electrical, ionic, and surface kinetics of the Mn_2O_3 nanofibers were enhanced due to the high surface area provided by the beads, temperature-induced lattice strain, and the ion buffering effect.

5. Acknowledgment

Muhamed Shareef Kolathodi gratefully acknowledges the IIT Madras, India for providing research infrastructures. Gurpreet Singh acknowledges financial support from National Science Foundation grant no. 1454151.

6. References

1. B. E. Conway, *Electrochemical supercapacitors: scientific fundamentals and technological applications*, Springer Science & Business Media, 2013.
2. M. Winter and R. J. Brodd, *Chemical reviews*, 2004, 104, 4245-4270.
3. P. Simon, Y. Gogotsi and B. Dunn, *Science Magazine*, 2014, 343, pp. 1210-1211.
4. J. R. Miller and A. F. Burke, *The Electrochemical Society Interface*, 2008, 17, 53.

5. V. Augustyn, P. Simon and B. Dunn, *Energy & Environmental Science*, 2014, 7, 1597-1614.

6. B. Conway, V. Birss and J. Wojtowicz, *Journal of Power Sources*, 1997, 66, 1-14.

7. C. Yuan, L. Yang, L. Hou, L. Shen, X. Zhang and X. W. Lou, *Energy & Environmental Science*, 2012, 5, 7883-7887.

8. G. Gao, H. B. Wu, S. Ding, L.-M. Liu and X. W. Lou, *Small*, 2015, 11, 804-808.

9. L. Zhang, H. B. Wu and X. W. Lou, *Chemical Communications*, 2012, 48, 6912-6914.

10. B. T. Zhu, Z. Wang, S. Ding, J. S. Chen and X. W. Lou, *RSC Advances*, 2011, 1, 397-400.

11. J. J. Yoo, K. Balakrishnan, J. Huang, V. Meunier, B. G. Sumpter, A. Srivastava, M. Conway, A. L. Mohana Reddy, J. Yu and R. Vajtai, *Nano Letters*, 2011, 11, 1423-1427.

12. L. L. Zhang and X. Zhao, *Chemical Society Reviews*, 2009, 38, 2520-2531.

13. K. Wang, H. Wu, Y. Meng and Z. Wei, *Small*, 2014, 10, 14-31.

14. T. Zhu, H. B. Wu, Y. Wang, R. Xu and X. W. Lou, *Advanced Energy Materials*, 2012, 2, 1497-1502.

15. T. Zhu, B. Xia, L. Zhou and X. Wen Lou, *Journal of Materials Chemistry*, 2012, 22, 7851-7855.

16. P. Simon and Y. Gogotsi, *Nature Materials*, 2008, 7, 845-854.

17. A. S. Arico, P. Bruce, B. Scrosati, J.-M. Tarascon and W. van Schalkwijk, *Nature Materials*, 2005, 4, 366-377.

18. T. Cottineau, M. Toupin, T. Delahaye, T. Brousse and D. Bélanger, *Applied Physics A*, 2006, 82, 599-606.

19. W. Deng, X. Ji, Q. Chen and C. E. Banks, *RSC Advances*, 2011, 1, 1171-1178.

20. G. Wang, L. Zhang and J. Zhang, *Chemical Society Reviews*, 2012, 41, 797-828.

21. M. S. Kolathodi and T. S. Natarajan, *Scripta Materialia*, 2015, 101, 84-86.

22. X. Wang, X. Wang, W. Huang, P. J. Sebastian and S. Gamboa, *Journal of Power Sources*, 2005, 140, 211-215.

23. M.-K. Song, S. Cheng, H. Chen, W. Qin, K.-W. Nam, S. Xu, X.-Q. Yang, A. Bongiorno, J. Lee, J. Bai, T. A. Tyson, J. Cho and M. Liu, *Nano Letters*, 2012, 12, 3483-3490.

24. W. Xiao, J. S. Chen and X. W. Lou, *CrystEngComm*, 2011, 13, 5685-5687.

25. W. Wei, X. Cui, W. Chen and D. G. Ivey, *Chemical Society Reviews*, 2011, 40, 1697-1721.

26. M. M. Najafpour, M. Hołyńska and S. Salimi, *Coordination Chemistry Reviews*, 2015, 285, 65-75.

27. Y.-Z. Long, M.-M. Li, C. Gu, M. Wan, J.-L. Duvail, Z. Liu and Z. Fan, *Progress in Polymer Science*, 2011, 36, 1415-1442.

28. W. Xiao, D. Hu, C. Peng and G. Z. Chen, *ACS Applied Materials & Interfaces*, 2011, 3, 3120-3129.

29. Y. Zhang, H. Feng, X. Wu, L. Wang, A. Zhang, T. Xia, H. Dong, X. Li and L. Zhang, *International Journal of Hydrogen Energy*, 2009, 34, 4889-4899.

30. C.-K. Lin, K.-H. Chuang, C.-Y. Lin, C.-Y. Tsay and C.-Y. Chen, *Surface and Coatings Technology*, 2007, 202, 1272-1276.

31. Z. Dong, S. J. Kennedy and Y. Wu, *Journal of Power Sources*, 2011, 196, 4886-4904.

32. C. K. Lin, C. H. Wu, C. Y. Tsai, C. Y. Chen and S. C. Wang, *Surface and Coatings Technology*, 2010, 205, 1595-1598.

33. K. Mondal, C.-Y. Tsai, S. Stout and S. Talapatra, *Materials Letters*, 2015, 148, 142-146.

34. W. Chen, Z. Fan, L. Gu, X. Bao and C. Wang, *Chemical Communications*, 2010, 46, 3905-3907.

35. E. Lee, T. Lee and B.-S. Kim, *Journal of Power Sources*, 2014, 255, 335-340.

36. W. Li, J. Shao, Q. Liu, X. Liu, X. Zhou and J. Hu, *Electrochimica Acta*, 2015, 157, 108-114.

37. K.-W. Park, *Journal of Materials Chemistry A*, 2014, 2, 4292-4298.

38. Y. Ding, C. Hou, B. Li and Y. Lei, *Electroanalysis*, 2011, 23, 1245-1251.

39. C. Shao, H. Guan, Y. Liu, X. Li and X. Yang, *Journal of Solid State Chemistry*, 2004, 177, 2628-2631.

40. C.-C. Hu and T.-W. Tsou, *Electrochemistry Communications*, 2002, 4, 105-109.

41. C. Zhang, L. Han, W. Liu, H. Yang, X. Zhang, X. Liu and Y. Yang, *CrystEngComm*, 2013, 15, 5150-5155.

42. J. H. Lee, Y. J. Sa, T. K. Kim, H. R. Moon and S. H. Joo, *Journal of Materials Chemistry A*, 2014, 2, 10435-10443.

43. P.-C. Hsu, H. Wu, T. J. Carney, M. T. McDowell, Y. Yang, E. C. Garnett, M. Li, L. Hu and Y. Cui, *ACS Nano*, 2012, 6, 5150-5156.

44. H. Shao, X. Zhang, S. Liu, F. Chen, J. Xu and Y. Feng, *Materials Letters*, 2011, 65, 1775-1777.

45. P. Scardi, M. Leoni and R. Delhez, *Journal of Applied Crystallography*, 2004, 37, 381-390.

46. A. Monshi, M. R. Foroughi and M. R. Monshi, *World Journal of Nano Science and Engineering*, 2012, 2, 154-160.

47. V. Mote, Y. Purushotham and B. Dole, *Journal of Theoretical and Applied Physics*, 2012, 6, 1-8.

48. A. K. Zak, W. A. Majid, M. E. Abrishami and R. Yousefi, *Solid State Sciences*, 2011, 13, 251-256.

49. S. Li, M. S. Sellers, C. Basaran, A. J. Schultz and D. A. Kofke, *International Journal of Molecular Sciences*, 2009, 10, 2798-2808.

50. E. Levi and D. Aurbach, *Solid State Ionics*, 2014, 264, 54-68.

51. C. Q. Sun, *Progress in Materials Science*, 2009, 54, 179-307.

52. P. Strasser, S. Koh, T. Anniyev, J. Greeley, K. More, C. Yu, Z. Liu, S. Kaya, D. Nordlund, H. Ogasawara, M. F. Toney and A. Nilsson, *Nature Chemistry*, 2010, 2, 454-460.

53. M.-W. Xu, D.-D. Zhao, S.-J. Bao and H.-L. Li, *Journal of Solid State Electrochemistry*, 2007, 11, 1101-1107.

54. Y.-F. Han, F. Chen, Z. Zhong, K. Ramesh, L. Chen and E. Widjaja, *The Journal of Physical Chemistry B*, 2006, 110, 24450-24456.

55. J. Xu, Y.-Q. Deng, Y. Luo, W. Mao, X.-J. Yang and Y.-F. Han, *Journal of Catalysis*, 2013, 300, 225-234.

56. Z. W. Chen, J. K. L. Lai and C. H. Shek, *Journal of Non-Crystalline Solids*, 2006, 352, 3285-3289.

57. Y. Luo, Y.-Q. Deng, W. Mao, X.-J. Yang, K. Zhu, J. Xu and Y.-F. Han, *The Journal of Physical Chemistry C*, 2012, 116, 20975-20981.

58. D. T. Zahn, *Physical Chemistry Chemical Physics*, 1999, 1, 185-190.

59. M. A. Stranick, *Surface Science Spectra*, 1999, 6, 39-46.

60. M. C. Biesinger, B. P. Payne, A. P. Grosvenor, L. W. M. Lau, A. R. Gerson and R. S. C. Smart, *Applied Surface Science*, 2011, 257, 2717-2730.

61. A. L. M. Reddy, M. M. Shaijumon, S. R. Gowda and P. M. Ajayan, *Nano Letters*, 2009, 9, 1002-1006.

62. J. Lee, M. C. Orilall, S. C. Warren, M. Kamperman, F. J. DiSalvo and U. Wiesner, *Nature Materials*, 2008, 7, 222-228.

63. M. D. Stoller and R. S. Ruoff, *Energy & Environmental Science*, 2010, 3, 1294-1301.

64. M. S. Kolathodi, M. Palei and T. S. Natarajan, *Journal of Materials Chemistry A*, 2015, 3, 7513-7522.

65. L. Athouël, F. Moser, R. Dugas, O. Crosnier, D. Bélanger and T. Brousse, *The Journal of Physical Chemistry C*, 2008, 112, 7270-7277.

66. M. Kim, Y. Hwang and J. Kim, *Journal of Materials Science*, 2013, 48, 7652-7663.

67. X. Xu, L. Pan, Y. Liu, T. Lu, Z. Sun and D. H. C. Chua, *Scientific Reports*, 2015, 5, 8458.

68. A. Sarkar, A. Kumar Satpati, V. Kumar and S. Kumar, *Electrochimica Acta*, 2015, 167, 126-131.

69. M. Liu, L. Gan, W. Xiong, Z. Xu, D. Zhu and L. Chen, *Journal of Materials Chemistry A*, 2014, 2, 2555-2562.

70. T.-H. Wu, D. Hesp, V. Dhanak, C. Collins, F. Braga, L. J. Hardwick and C.-C. Hu, *Journal of Materials Chemistry A*, 2015, 3, 12786-12795.

71. R. Lamber, N. Jaeger and G. Schulz-Ekloff, *Surface Science*, 1990, 227, 15-23.

72. L. Yang, S. Cheng, Y. Ding, X. Zhu, Z. L. Wang and M. Liu, *Nano Letters*, 2011, 12, 321-325.

73. M. S. Hong, S. H. Lee and S. W. Kim, *Electrochemical and Solid-State Letters*, 2002, 5, A227-A230.

74. V. Khomenko, E. Raymundo-Piñero and F. Béguin, *Journal of Power Sources*, 2006, 153, 183-190.

75. K. Jurewicz, E. Frackowiak and F. Béguin, *Applied Physics A*, 2004, 78, 981-987.

76. Q. T. Qu, B. Wang, L. C. Yang, Y. Shi, S. Tian and Y. P. Wu, *Electrochemistry Communications*, 2008, 10, 1652-1655.

77. M. R. Lukatskaya, O. Mashtalir, C. E. Ren, Y. Dall'Agnese, P. Rozier, P. L. Taberna, M. Naguib, P. Simon, M. W. Barsoum and Y. Gogotsi, *Science*, 2013, 341, 1502-1505.

78. H. Su, Y.-F. Xu, S.-C. Feng, Z.-G. Wu, X.-P. Sun, C.-H. Shen, J.-Q. Wang, J.-T. Li, L. Huang and S.-G. Sun, *ACS Applied Materials & Interfaces*, 2015, 7, 8488-8494.

Beaded Manganese Oxide (Mn_2O_3) Nanofibers: Preparation and Application for Capacitive Energy Storage

Muhamed Shareef Kolathodi[1,3*], Samerender Nagam Hanumantha Rao[1,2], Tirupattur Srinivasan Natarajan[1], Gurpreet Singh[3]

[1]*Conducting Polymer Lab, Department of Physics, Indian Institute of Technology Madras, Chennai - 600036, India Fax: +91- 44 22574852; Tel: +91- 4422574860;*

[*]*Email: muhamed@ksu.edu*

[2]*Department of Biomedical Engineering, Michigan Technological University, Houghton, MI 49931, USA*

[3]*Department of Mechanical and Nuclear Engineering, Kansas State University, Manhattan, Kansas 66506, United States Tel.: +1-785-532-7085; Fax: +1-785-532-7057.*

Graphical abstract